A Tough, Adhesive, and Protective Binder Shield for Stabilizing High-Nickel Cathodes in Lithium-Ion Batteries

*Yeong Hun Jeong, Gwangbin Won, Seunghyeon Kim, Min Seo Jo, Sinyoung Seo, Daun Jeong, and Jimin Shim**

High-nickel layered oxide cathodes, $LiNi_xCo_yMn_zO_2$ (NCM), offer high theoretical capacities and energy densities but suffer from structural degradation and interfacial instability, limiting their practical application in lithium-ion batteries. To address these challenges, a tough, adhesive, and protective binder is developed based on polyacrylic acid (PAA)-grafted polyvinylidene fluoride (PVDF) cross-linked with branched polyethyleneimine (PEI) (PVDFA-N). Systematic tuning of the binder composition enables precise control over mechanical properties and the establishment of structure-property-performance relationships. The optimized PVDFA-N binder exhibits high toughness and strong adhesion, delivering excellent electrochemical performance even under high mass loading and lean binder conditions. Post-mortem analyses and density functional theory (DFT) calculations reveal that strong interfacial adhesion and the presence of chelating functional groups allow the binder to act as a protective shield, effectively suppressing structural degradation, transition metal ion dissolution, and inhomogeneous cathode-electrolyte interphase (CEI) formation. Moving beyond the conventional role of mechanical adhesion, this study establishes a new paradigm for binder design by highlighting the active role of the binder in surface protection, offering a promising pathway toward durable, high-energy lithium-ion batteries.

1. Introduction

To meet the increasing demand for high-energy-density lithium-ion battery systems across various industries, significant efforts have been made to develop high-capacity electrode materials.[1–3] High-nickel layered oxide cathodes, $LiNi_xCo_yMn_zO_2$ (NCM, $x > 0.8$), have been recognized as promising materials primarily due to their high specific capacity and energy density.[4] However, while increasing the Ni content in NCM enhances specific capacity, it also compromises cycling stability due to structural degradation of NCM.[4–6] In particular, NCM undergoes anisotropic volume changes during cycling, caused by the phase transition at ≈4.2 V, which triggers the formation of internal microcracks that facilitate electrolyte penetration and subsequent side reactions.[7,8] The reduction of highly reactive $Ni^{3+/4+}$ species to Ni^{2+} accelerates structural degradation by triggering oxygen release and the formation of resistive NiO-type rock-salt phases, driven by cation mixing between Ni^{2+} and Li^+.[9,10] Additionally, the dissolution of transition metals from the NCM cathode and their subsequent migration to the anode further contribute to capacity fading.[10] This parasitic degradation cycle leads to increased electrolyte decomposition and an unstable cathode-electrolyte interphase (CEI).[11,12] To mitigate these issues, extensive research has focused on optimizing the design of active materials. Key strategies include introducing Ni concentration gradients,[13,14] doping with metallic elements or anions at cation or oxygen sites,[15,16] and applying protective coatings.[17,18]

In addition to addressing NCM degradation, preparing high-thickness electrodes must be pursued in parallel to achieve high energy density.[19,20] Significant progress has been made in fabricating ultrathick electrodes by optimizing binder and electrode composition,[21,22] modifying electrode slurry viscoelasticity,[23,24] and controlling pressure and sintering temperature during electrode preparation.[25,26] Among these strategies, selecting appropriate binder materials with strong adhesiveness is crucial for maintaining the structural integrity of cathode components, particularly when incorporating high active material loadings.[27–29] Polyvinylidene fluoride (PVDF), the most commonly used cathode binder, has proven inadequate for ensuring cycling stability in thick electrodes due to its insufficient adhesive properties.[22] While research has focused on enhancing binder adhesion through functional group engineering,[30,31] covalent cross-linking,[32,33] and copolymerization,[22] most studies have concentrated solely on enhancing the adhesive strength of binder materials. However, a key open question remains: what combination of mechanical properties, including both adhesive and tensile properties, is necessary to enable thick electrodes

---

Y. H. Jeong, G. Won, S. Kim, M. S. Jo, S. Seo, J. Shim
Department of Chemistry Education
Seoul National University
1 Gwanak-ro, Gwanak-gu, Seoul 08826, Republic of Korea
E-mail: jiminshim@snu.ac.kr

D. Jeong
Department of Chemical Engineering and Materials Science
University of Minnesota
Minneapolis, MN 55455, USA

The ORCID identification number(s) for the author(s) of this article can be found under https://doi.org/10.1002/aenm.202502765

DOI: 10.1002/aenm.202502765

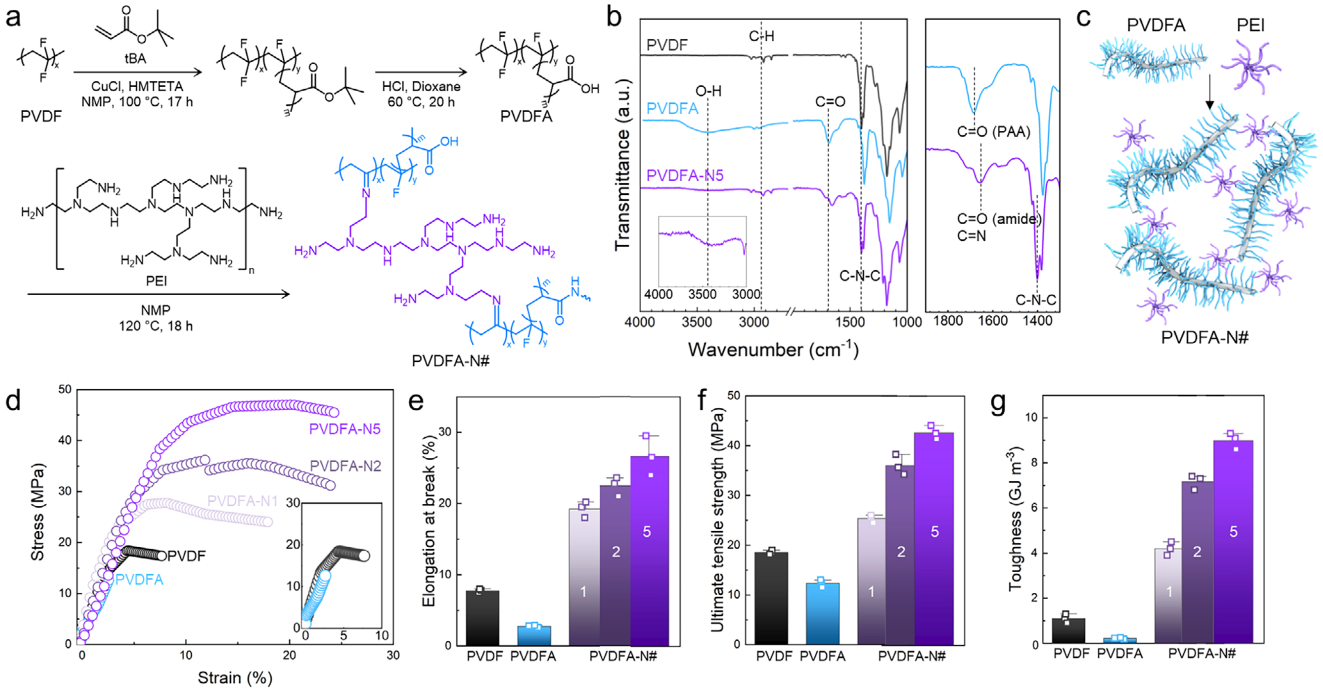

Figure 1. Molecular characterizations and tensile properties of a series of PVDFA-N#. a) Synthetic route of PVDFA-N#, where # indicates the mol% of ethyleneimine groups in PEI along the VDF repeating units of PVDFA. b) FT-IR spectra of PVDF, PVDFA, and PVDFA-N5 (left) and magnified region of PVDFA and PVDFA-N5 (right). c) Schematic illustration of the PVDFA-N# binder composed of PVDFA and PEI. d) Stress–strain curves of PVDF, PVDFA, and PVDFA-N# and the resulting e) elongation at break, f) ultimate tensile strength, and g) toughness determined by the stress–strain curves.

without compromising cycling stability? In addition, it remains unclear whether binder design can effectively address the aforementioned NCM degradation issues by serving as a protective surface layer. Although the conventional role of binders is to provide mechanical cohesion within electrodes, they must evolve beyond mechanical support to actively function as protective shields at the electrode-electrolyte interface.

Herein, a tough, adhesive, and protective binder system, PVDFA-N#, is developed by grafting PAA onto PVDF, followed by cross-linking with PEI. By systematically tuning the cross-linking density, the mechanical properties and interfacial functionality of the PVDFA-N system are optimized. The optimized PVDFA-N5 binder enables the construction of crack-free, high-loading NCM cathodes, suppresses structural degradation and metal dissolution, and facilitates the formation of a thin, stable CEI. This study provides a new strategy for binder design, emphasizing the importance of achieving mechanical toughness, strong adhesion, and protective functionality to realize durable, high-energy lithium-ion batteries.

2. Results and Discussion

2.1. Molecular Design and Characterizations of PVDFA-N Binder System

To functionalize PVDF to impart advantageous binder properties, including adhesiveness and resilience, commercially available PVDF was first grafted with PAA, followed by cross-linking with branched PEI, as depicted in **Figure** 1a. The PAA-grafted PVDF (PVDF-g-PAA), referred to as PVDFA, was synthesized via atom transfer radical polymerization (ATRP) using *tert*-butyl acrylate (tBA) as the monomer. As confirmed by ^{1}H NMR analysis (Figure S1, Supporting Information), the molar percentage of tBA units along the PVDF backbone was 20%. The *tert*-butyl groups were then converted to carboxylic acid via acid-catalyzed hydrolysis, resulting in PVDFA, with nearly complete conversion. The resulting PVDFA was subsequently cross-linked with branched PEI, yielding PVDFA-N#, where # represents the molar percentage of ethyleneimine groups ($—CH_2—CH_2—N—$) in the PEI relative to the VDF repeating units ($—CH_2—CF_2—$). Thus, the cross-linking density of PVDFA-N# is increased as the # increases in the designation. The structure of PVDFA-N# was confirmed by FT-IR spectra in Figure 1b. After grafting PAA side chains onto PVDF, PVDFA exhibits characteristic O—H and C═O stretching peaks at ≈3400 and 1700 cm^{-1}, respectively. Upon cross-linking with PEI, a C—N—C stretching peak emerges at 1400 cm^{-1}, while the C═O stretching peaks of PVDFA are rearranged due to the incorporation of amide and imine bond signals ≈1640 cm^{-1}.[34–36] Figure 1c illustrates the molecular cartoon of the cross-linked PVDFA-N# binder structure. The PVDF backbone provides essential binder properties, such as electrochemical stability and mechanical strength. Grafting with PAA introduces carboxylic acid groups in the side chains, which enhance adhesion properties primarily through hydrogen bonding with active materials in the electrode. Additionally, the cross-linked structure of PVDFA-N# enabled by PEI improves mechanical properties, including tensile strength and toughness, which help maintain the structural integrity of electrodes during long-term cycling. As shown in the stress–strain curves (Figure 1d), PVDFA is more rigid than pristine PVDF, exhibiting brittle failure at the very beginning

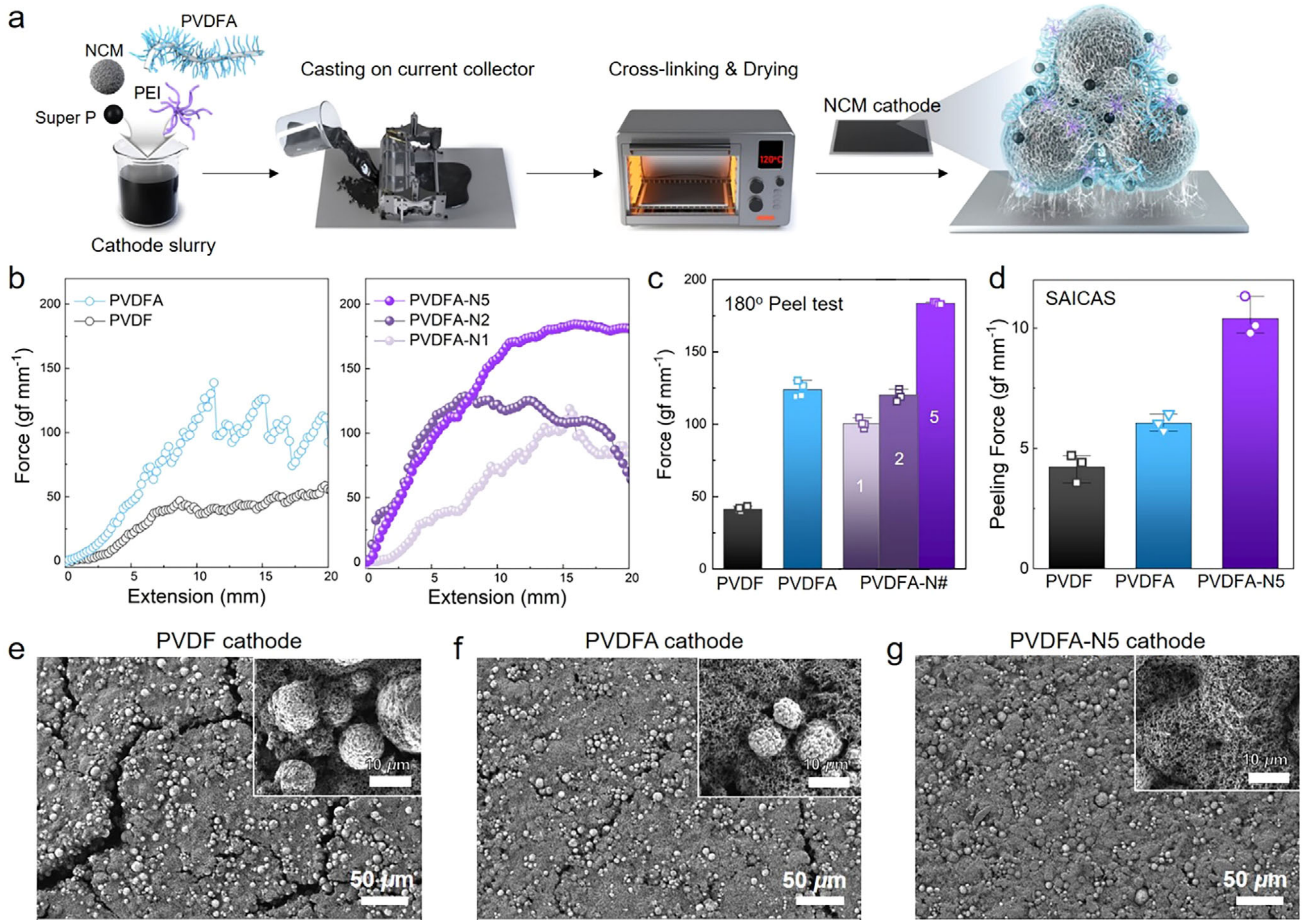

Figure 2. Preparation and adhesion properties of NCM cathodes. a) Schematic illustration of preparing NCM cathodes prepared with PVDFA-N#. b) 180° peel test profiles and the resulting c) average peel strength of NCM cathodes prepared with PVDF, PVDFA, and PVDFA-N#. d) Peeling force values of NCM cathodes with PVDF, PVDFA, and PVDFA-N5 determined by SAICAS. Top-view SEM images of NCM cathodes prepared with e) PVDF, f) PVDFA, and g) PVDFA-N5. The mass loading of the active materials in the NCM cathode is ≈10–11 mg cm^{-2}, with a NCM: Super P: binder composition of 8:1:1 (wt.%).

of stretching without undergoing plastic deformation. This behavior is likely due to intermolecular hydrogen bonding, which restricts the movement of PAA side chains, preventing them from sliding past one another under stress and thereby limiting stretchability.[37,38] Interestingly, PVDFA-N# demonstrates a dramatic increase in elongation at break, with this effect becoming more pronounced as cross-linking density increases (Figure 1e). Additionally, the ultimate tensile strength of PVDFA-N# is significantly higher than that of both PVDF and PVDFA, substantially improving overall toughness (Figure 1f,g). It is interesting to note that even a small amount of PEI cross-linker significantly enhances tensile properties, likely due to the existence of physical entanglements within the network induced by the polymeric cross-linker.[39,40]

2.2. Effect of Binders on Adhesion Properties of NCM Cathodes

Figure 2a illustrates the fabrication process of NCM cathodes incorporating PVDFA-N# binders. The cathode slurry, composed of NCM, Super P, PVDFA, and PEI, is cast onto an aluminum current collector. During the subsequent drying step at 120 °C, in situ cross-linking between PVDFA and PEI occurs. In the final NCM cathode, both the NCM particles and conductive additives are uniformly dispersed and encapsulated by the cross-linked PVDFA-N network, which also promotes strong adhesion to the current collector.[41–43]

To investigate the effect of the PVDFA-N# binder on the adhesion properties of NCM cathodes, a 180° peel test was conducted on NCM cathodes prepared with PVDF, PVDFA, and PVDFA-N# (Figure 2b). As summarized in Figure 2c, PVDFA exhibited a peel strength approximately three times greater than that of PVDF, primarily due to the enhanced adhesion provided by the carboxylic acid moieties, which promote hydrogen bonding with both NCM and the aluminum current collector.[44–46] However, in the case of PVDFA-N1, the addition of the PEI cross-linker to PVDFA induces a significant decrease in peel strength. This decrease is likely due to the reduction in carboxylic acid groups, which react with PEI to form imine and amide linkages. Despite this, the peel strength of PVDFA-N# remained higher than that of PVDF, and it increased progressively with higher cross-linking density. Specifically, PVDFA-N2 achieved a peel strength comparable to PVDFA, while PVDFA-N5 demonstrated an even higher peel strength than PVDFA. We speculate that the recovery in adhesion strength with increasing cross-linking density in PVDFA-N# is due to the formation of a robust network structure that strongly bonds with the electrode components.[39–41] Additionally, since the tensile behavior closely mirrors the peel strength results, the enhanced toughness of the network likely contributes to improved adhesion properties.[38] As shown in the photographs in Figure S2 (Supporting Information), most of the cathode composite layer in PVDFA-N5 remains intact after the peel test, with minimal material left on the tape, whereas that of the PVDF cathode is nearly completely detached from the current collector. Since the 180° peel test primarily assesses the weakest interfacial adhesion site where mechanical delamination occurs,[47] we also performed surface and interfacial cutting analysis system (SAICAS) analysis to evaluate the adhesion properties of NCM cathodes within the cathode composite layer (see Figure S3, Supporting Information for the representative SAICAS profiles). As summarized in Figure 2d, the peeling force measured by SAICAS followed a similar trend to that observed in the 180° peel test. However, the difference between PVDF and PVDFA was much smaller in the SAICAS result, likely because the hydrogen bonding between the binder and current collector is not accounted for in this method.[22] However, PVDFA-N5 still exhibited a peeling force more than twice as high as that of the pristine PVDF, indicating excellent adhesion between the cathode components in the composite layer. Note that increasing the PEI content beyond that of PVDFA-N5 significantly reduced the solubility in NMP, making it difficult to achieve uniform electrode fabrication. As shown in the SEM images (Figure 2e–g), the distinct adhesion properties lead to significant morphological changes in the cathodes. The PVDF cathode exhibits numerous large cracks, and some NCM particles are not well adhered to each other. The PVDFA cathode partially addresses this issue, but still contains a few cracks and areas where NCM particles are not fully covered by the binder. In sharp contrast, the PVDFA-N5 cathode displays a uniformly distributed composite layer with no cracks, where the NCM particles are completely encased in the PVDFA-N5 binder network. The SEM images of the cathodes from the other PVDFA-N# series are shown in Figure S4 (Supporting Information).

2.3. Roles of Binders in Determining Cycling Performance Under Various Conditions

The cycling performance of Li/NCM811 cells with PVDF, PVDFA, and PVDFA-N# binders was evaluated, as shown in **Figure 3a** (see the voltage-capacity profiles in Figure S5, Supporting Information). It was observed that cells with PVDFA, PVDFA-N1, and PVDFA-N2 exhibited inferior cycling performance compared to the PVDF cell, as their capacity decayed much earlier. Contrary to our expectations, the highly adhesive PVDFA and PVDFA-N2 failed to surpass PVDF in both capacity retention and overall capacity values. However, PVDFA-N5 demonstrated an exceptionally long lifespan of over 600 cycles, with ≈80% capacity retention after 300 cycles. This performance surpasses that of most previously reported coating or binder strategies for NCM811 cathodes under similar conditions (Table S1, Supporting Information). Although the PVDF cathode exhibited higher capacities in the early cycles due to its linear architecture and facile electrolyte uptake, the PVDFA-N5 cathode, comprising a robust, cross-linked network, gradually outperformed it by forming a stable interfacial layer that mitigates degradation over long-term cycling. Additionally, the cycled PVDFA-N5 cathode preserved its pristine appearance, while the outer layer of the PVDF cathode had delaminated from the current collector and adhered to the separator (Figure S6, Supporting Information). To reveal the impact of the physical properties of the binders on cycling performance, we plotted the relationship between cycle life of the cells and the physical properties of each binder, as shown in Figure 3b. The cycle life was defined as the point at which the coulombic efficiency spiked. The PVDFA cell exhibited a shorter lifespan than the PVDF cell, despite having ≈3 times the peel strength. This is likely due to the decreased toughness value as discussed earlier. Grafting PAA onto PVDF makes the material more brittle and less tough, compromising the overall structural integrity of the cathodes during long-term cycling.[32] When cross-linked with PEI, PVDFA-N1 showed improved toughness compared to PVDFA. However, the reduced adhesiveness offsets the benefits of increased toughness, resulting in a cycle life similar to that of PVDFA. As the cross-linking density increased further, PVDFA-N2 and PVDFA-N5 showed significant improvements in both peel strength and toughness, leading to a gradual increase in cycle life. It is interesting to note that both the peel strength and toughness of the binders simultaneously influence the cycling performance of the cells. As shown in Figure S7 (Supporting Information), the PVDFA-N5 binder enabled slightly enhanced rate performance compared to PVDF, primarily due to better mechanical cohesion and connectivity. Furthermore, the PVDFA-N5 cell demonstrated significantly lower CEI and charge transfer resistances compared to the PVDF cell after cycling (Figure 3c), as indicated by the first and second semi-circles in the Nyquist plot, respectively. Although the initial impedance of the PVDFA-N5 cathode was relatively high due to the dense and partially inactive cross-linked polymer network, the interfacial resistance gradually decreased during cycling as the binder conformed to the particle surfaces and formed a stable CEI layer. This suggests that the highly adhesive PVDFA-N5 forms a thin, intimate coating over the NCM, effectively passivating the NCM surface without deteriorating charge transfer kinetics. To support the improved charge transport properties, galvanostatic intermittent titration technique (GITT) analysis revealed that the PVDFA-N5 cathode exhibited higher Li^+ diffusion coefficients (D_{Li^+}) and lower internal resistance compared to PVDF across most state-of-charge (SOC) regions (Figure S8, Supporting Information).[32,48] To further investigate structural evolution during cycling, differential capacity (dQ dV^{-1}) analysis was performed (Figure S9, Supporting Information), revealing that the PVDFA-N5 binder effectively preserves the H2–H3 phase transition behavior even after prolonged cycling, in contrast to the progressive peak fading observed with the PVDF binder.[48,49]

To further evaluate the practical viability of PVDFA-N5 as a binder material, its cycling performance was tested under harsher conditions and compared with PVDF. Figure 3d shows the cycling performance of PVDFA and PVDFA-N5 cells, where

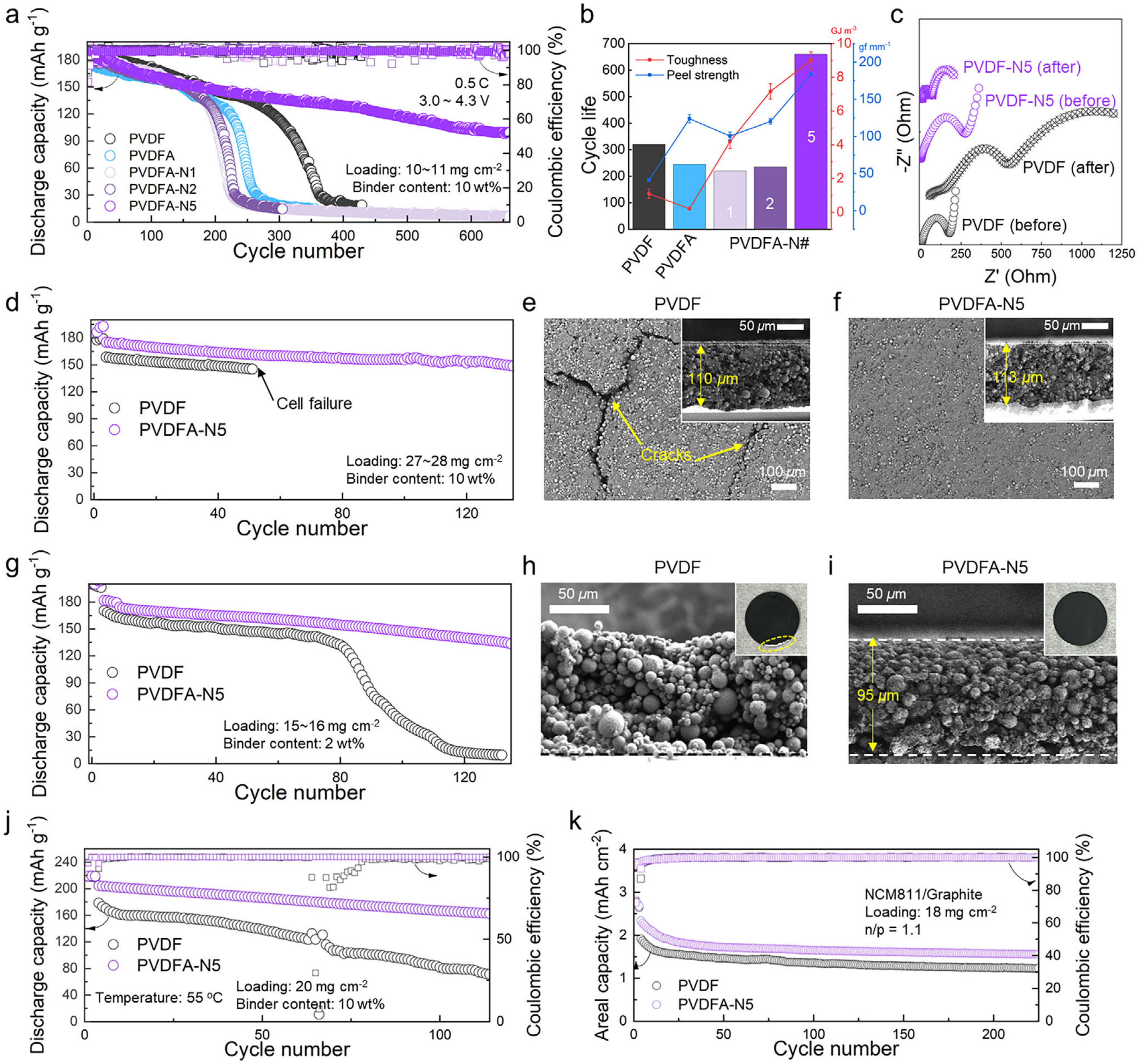

Figure 3. Cycling performance under 0.5 C at 30 °C within the voltage range of 3.0–4.3 V. The cells were subjected to formation steps, cycled under 0.1 C for 3 cycles before the main cycling. a) Long-term cycling performance of the cells with PVDF, PVDFA, and PVDFA-N# (active material loading: 10–11 mg cm^{-2}). b) Relationship between the cycle life of the cells and physical properties (toughness and peel strength) of binders. c) Nyquist plots of the cells with PVDF and PVDFA-N5 before and after cycling. d) Cycling performance of PVDF and PVDFA-N5 cathodes with high mass loading (27–28 mg cm^{-2}). Surface and cross-sectional (inset) SEM images of the NCM cathodes prepared with e) PVDF and f) PVDFA-N5 with high mass loading. g) Cycling performance of PVDF and PVDFA-N5 cathodes with lean binder condition (2 wt.%) and the corresponding cross-sectional SEM images of the cathodes prepared with h) PVDF and i) PVDFA-N5 (inset: optical photographs of each cathode). j) Cycling performance of PVDF and PVDFA-N5 cathodes at 55 °C (mass loading: 20 mg cm^{-2}). k) NCM811/graphite full cell cycling performance (mass loading: 18 mg cm^{-2}, n/p = 1.1).

the areal mass loading of NCM was increased ≈3 fold to ≈27–28 mg cm^{-2}. The corresponding cathode thickness at this loading was ≈110 µm, as observed in the inset SEM images in Figure 3e,f. Under these conditions, the PVDFA-N5 cell exhibited stable cycling performance over 140 cycles, whereas the PVDF cell failed after only 50 cycles. Given that the SEM analysis (Figure 3e,f) reveals extensive cracking in the PVDF cathode, whereas the PVDFA-N5 cathode maintains a compact morphology with evenly distributed components, the high adhesive strength and toughness of PVDFA-N5 are key to forming stable, thick cathodes that maintain structural integrity and deliver superior cycling performance.[32,33] Additionally, the cycling performance of the cathodes prepared with a low binder content of 2 wt.% was evaluated (Figure 3g). Despite the lean binder condition, the PVDFA-N5 cell exhibited excellent capacity retention over 130 cycles, whereas the PVDF cell showed significant

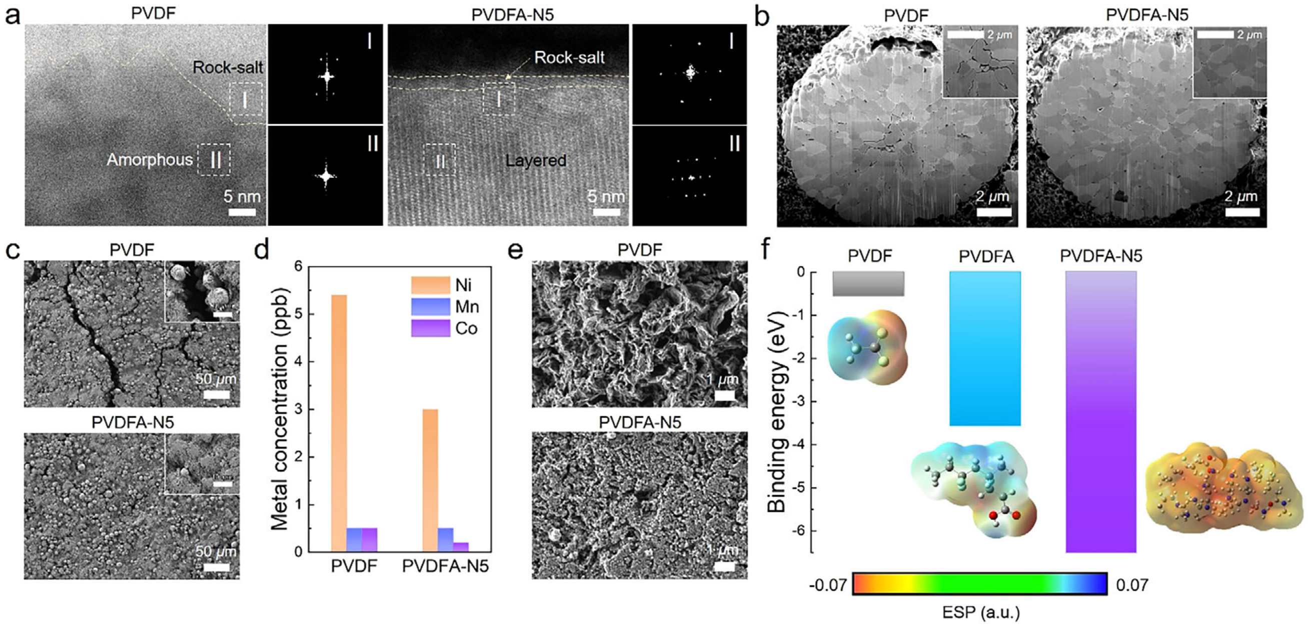

Figure 4. Post-mortem analysis of the cycled NCM cathodes prepared with PVDF and PVDFA-N5 after 300 cycles under 0.5 C at 30 °C within the voltage range of 3.0–4.3 V. a) STEM images and the corresponding fast Fourier transform (FFT) patterns of the PVDF and PVDFA-N5 cathode. b) Cross-sectional FIB-SEM images and c) top-view SEM images of the PVDF and PVDFA-N5 cathode. d) Concentration of Ni, Mn, and Co ions deposited on the surface of Li metal from PVDF and PVDFA-N5 cells determined by ICP-MS. e) Top-view SEM images of the Li metal anodes retrieved from the PVDF and PVDFA-N5 cells. f) DFT-calculated binding energies of PVDF, PVDFA, and PVDFA-N5 with Ni^{2+} and their electrostatic potential maps.

capacity degradation after 80 cycles. Optical images of the pristine cathodes (insets in Figure 3h,i) revealed that the composite layer of the PVDF cathode delaminated during the punching process, even before cycling. Cross-sectional SEM images of the cathodes further indicated an uneven distribution of NCM particles in the PVDF cathode, reflecting poor cohesion among the electrode components (see the EDS maps in Figure S10a, Supporting Information). In addition, the top portion of the PVDF cathode peeled off during vacuum processing for SEM imaging, likely due to insufficient binder adhesion. In sharp contrast, the PVDFA-N5 cathode maintained a homogeneous cross-section with uniformly distributed NCM particles (see the EDS maps in Figure S10b, Supporting Information), highlighting the superior adhesive properties of the PVDFA-N5 binder. To further evaluate the thermal stability of the binders, cycling tests were conducted at 55 °C (Figure 3j). The PVDFA-N5 cell exhibited stable capacity retention and suppressed Coulombic efficiency fluctuations compared to the PVDF cell, confirming its superior structural and interfacial stability under elevated temperatures. This improvement is attributed to the accelerated degradation of Ni-rich cathodes at elevated temperatures, which is effectively mitigated by the strong adhesion and thermally stable cross-linked architecture of the PVDFA-N5 binder, forming a protective shield on the NCM surface. Figure 3k shows the cycling performance of NCM811/graphite full cells with a mass loading is 18 mg cm^{-2} and an n/p ratio of 1.1. Although both cells exhibited an initial drop in capacity during the transition from the 0.1 C formation step to main cycling at 0.5 C, the PVDFA-N5 cell consistently outperformed the PVDF cell in terms of capacity over 200 cycles.

2.4. Post-mortem Analyses of the Cycled NCM Cathodes and Li Metal

To elucidate the structural and interfacial stability of the NCM cathodes imparted by the binder, post-mortem analysis was conducted on the cycled NCM cathodes. As shown in the high-resolution STEM images (**Figure** 4a; Figure S11, Supporting Information), the PVDF cathode experienced significant surface reconstruction, exhibiting an amorphous layer and rock-salt phase indicative of severe structure degradation.[21,50] In contrast, the PVDFA-N5 cathode retained the layered crystal structure with only a thin rock-salt phase on the surface, suggesting effective suppression of structural collapse.[22] Cross-sectional FIB-SEM images (Figure 4b) further revealed the formation of internal microcracks within the NCM particles in the PVDF cathode, which are typically associated with cumulative lattice strain and oxygen release during long-term cycling.[51,52] Remarkably, such microcracks were absent in the PVDFA-N5 cathode, indicating its ability to preserve mechanical and structural integrity. Furthermore, XRD patterns of cycled cathodes (Figure S12, Supporting Information) show that the PVDFA-N5 binder effectively preserves the layered structure of NCM811, while severe structural degradation is observed in the PVDF cathode. Top-view SEM images of the cathode surface after cycling (Figure 4c) also confirmed that the PVDFA-N5 cathode maintained a crack-free and well-adhered morphology, whereas the PVDF cathode exhibited extensive surface cracking and delamination. These results demonstrate that the PVDFA-N5 binder acts as a protective interfacial shield that mitigates mechanical failure and electrode disintegration. TEM analysis (Figure S13, Supporting Information) further revealed that the PVDFA-N5 binder forms a uniform, conformal nanoscale film on the surface of NCM811 particles, supporting its role as a protective shield, while PVDF does not form any discernible coating and merely acts as a physical connector between particles.

The protective role of the binder was also evident on the Li metal anode side, as further confirmed by quantifying transition metal crossover. As shown in Figure 4d, the concentration of Ni, Mn, and Co ions deposited on the Li surface was significantly lower in the PVDFA-N5 cell compared to the PVDF cell. This result indicates that the PVDFA-N5 binder effectively coordinates transition metal ions at the cathode side, suppressing their migration toward the anode.[53] The strong coordination capability arises from the abundance of carboxylic acid groups in the PVDFA and amine groups in the branched PEI, both of which can effectively chelate metal ions.[51,54] As a result of this reduced metal crossover, the morphology of Li deposition was also significantly affected, as observed in the SEM images (Figure 4e). The PVDF cell exhibited porous and uneven dendritic Li structures, while the PVDFA-N5 cell showed densely packed and uniform Li deposits. This clear contrast highlights that binder chemistry can also alter Li plating behavior by serving as an ion-trapping protective shield. To further validate this chelation mechanism, density functional theory (DFT) calculations were conducted to determine the binding energies between Ni^{2+} ions and the binders (Figure 4f). The PVDFA binder exhibited stronger binding to Ni^{2+} than PVDF, which can be attributed to multiple carboxyl groups forming coordination complexes.[55] Interestingly, PVDFA-N5 showed an even lower binding energy, suggesting enhanced chelation likely due to the nitrogen atoms in the branched PEI structure.[56,57] To complement the Ni^{2+} binding analysis, additional DFT calculations were performed, revealing that PVDFA-N5 also forms strong chelation with Mn^{2+} (−7.3 eV) and Co^{2+} (−9.5 eV), thereby supporting its ability to suppress the dissolution of all major transition metal ions (Figure S14, Supporting Information). The electrostatic potential (ESP) mapping also confirmed the presence of electron-rich domains, supporting the favorable coordination environment of PVDFA-N5. These results collectively demonstrate that the PVDFA-N5 binder acts as a protective shield, minimizing metal ion crossover and promoting uniform Li metal morphology.

2.5. Post-Mortem In-Depth Characterizations of the CEI Layers

To investigate the detailed chemical composition and spatial distribution of the species within the CEI layers on cycled NCM cathodes, in-depth post-mortem XPS and TOF-SIMS analyses were conducted. **Figure 5a** presents the XPS depth profiling results of the atomic ratios in the PVDF and PVDFA-N5 cathodes, obtained by Ar-ion etching. Notably, the PVDFA-N5 cathode exhibited significantly lower O and Ni content throughout the depth compared to the PVDF cathode. This suggests that PVDFA-N5 plays a crucial role in suppressing electrolyte decomposition and transition metal dissolution by providing protective coverage on the NCM surface.[22] Furthermore, as confirmed by DFT calculations, the presence of abundant carboxylic acid and amine moieties in PVDFA-N5 likely facilitates coordination with transition metal ions, effectively inhibiting their dissolution.[55] Additionally, the atomic composition of the CEI layers in the PVDFA-N5 cathode displayed a consistent pattern after 60 s of etching, whereas the PVDF cathode showed a more irregular distribution, highlighting the homogeneous nature of the CEI in the PVDFA-N5 cathode. As shown in the representative C1*s* spectra (Figure 5b,c), the PVDF cathode contains relatively larger amounts of C─O and C═O species than the PVDFA-N5 cathode, indicating more severe electrolyte decomposition.[55] Similarly, the F1*s* spectra reveal that the PVDF cathode has a stronger intensity of LiF, primarily attributed to the decomposition of $LiPF_6$ salt. Quantitatively, the CF_x: LiF ratio was 1:6.7 in the PVDF cathode, whereas it was significantly lower at 1:0.27 in the PVDFA-N5 cathode, indicating markedly suppressed LiF formation. The accumulation of LiF, known for its high resistivity, in the CEI can hinder electrochemical kinetics, leading to the reduced capacity retention observed in the PVDF cathode.[58] Moreover, since LiF formation is typically accompanied by the generation of hydrofluoric acid (HF), the PVDF cathode is more susceptible to accelerated transition metal dissolution, further deteriorating cycling performance.[59] In the Ni2*p* spectra, the Ni$2p_{3/2}$ region was deconvoluted into Ni^{2+} (852.4 eV) and Ni^{3+} (856.3 eV) components with different valence states. It was found that the PVDFA-N5 cathode exhibited a lower Ni^{2+}/Ni^{3+} ratio compared to the PVDF cathode, suggesting that cation mixing between Ni^{2+} and Li^+ was more effectively suppressed in the PVDFA-N5 cathode.[60]

To probe the 3D spatial distribution of CEI species in the cycled cathodes, TOF-SIMS analysis was performed. As shown in the depth profiles (Figure 5d,e), specific ionic species were selected to represent the decomposition products of the electrolyte. The C_2HO^- species originates from the decomposition of organic electrolyte components, while LiF_2^- and PO_2^- species are attributed to the decomposition of the inorganic $LiPF_6$ salt.[61] Note that a portion of LiF_2^- might also result from the ionization of the fluorinated binder matrix.[22] The PVDF cathode exhibited consistently high intensities of LiF_2^- and PO_2^- throughout the depth, whereas these signals declined beyond a certain depth in the PVDFA-N5 cathode. This observation suggests reduced electrolyte decomposition in the PVDFA-N5 cathode, corroborating the previously discussed XPS results. Since the outer CEI primarily consists of $LiPF_6$ decomposition products, its thickness was defined at the depth where PO_2^- intensity reached its maximum.[62] The inner CEI thickness was determined by the intersection point of the PO_2^- and Ni^- signals, where the bulk Ni signal becomes more prominent than that of the CEI species. Note that the colored bars in the depth profile indicate the boundaries between the outer and inner CEI layers. Interestingly, the overall CEI thickness of the PVDFA-N5 cathode was significantly thinner, approximately half that of the PVDF cathode. In particular, the inner CEI layer of the PVDF cathode comprised 86% of the total CEI thickness and was predominantly composed of organic species, such as C_2HO^-. In contrast, the PVDFA-N5 cathode showed a notably reduced inner CEI thickness. This can be attributed to the protective nature of PVDFA-N5, which effectively shields the NCM surface, thereby suppressing both electrolyte decomposition and structural degradation of the NCM.

These findings collectively emphasize the critical role of binder design in preserving cathode stability during long-term cycling, as illustrated in Figure 5f. In contrast to PVDF, which lacks sufficient surface adhesion and fails to protect the NCM surface,

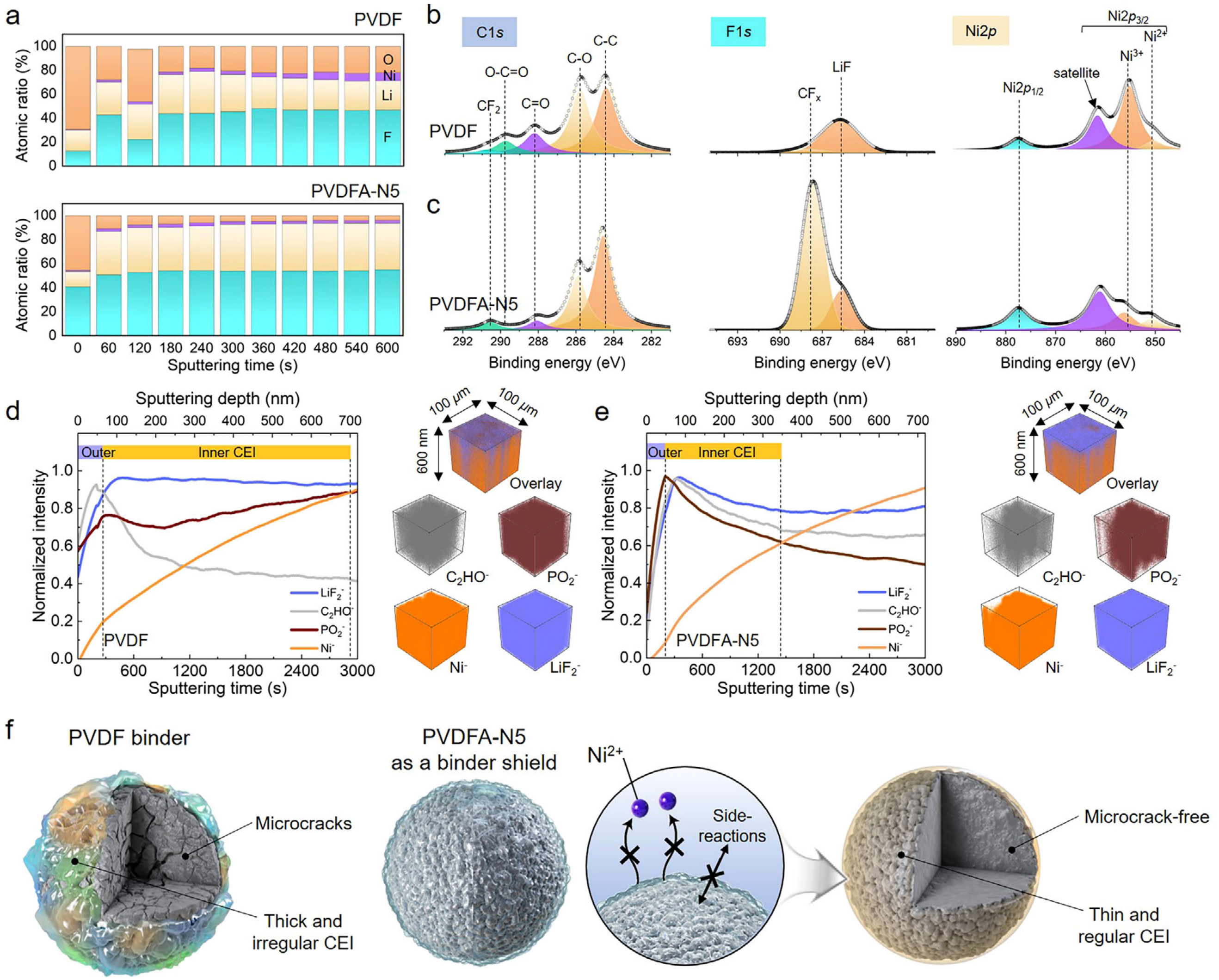

Figure 5. Post-mortem in-depth characterizations of the CEI layers on the cycled NCM cathodes prepared with PVDF and PVDFA-N5 after 300 cycles. a) In-depth XPS profiling of the atomic ratio of the PVDF and PVDFA-N5 cathode. Representative deconvoluted C1*s*, F1*s*, and Ni2*p* XPS spectra of the b) PVDF and c) PVDFA-N5 cathode. Normalized TOF-SIMS depth profiles of the d) PVDF and e) PVDFA-N5 cathode with 3D maps of the selected species and overlay images. f) Schematic illustration highlighting the role of the PVDFA-N5 as a protective shield.

leading to microcrack formation and the development of a thick and irregular CEI, the PVDFA-N5 strongly adheres to the NCM surface and forms a robust, conformal coating that functions as a multifunctional protective shield. Its strong interfacial adhesion to the NCM surface, coupled with effective chelation of dissolved transition metal ions, prevents their migration and suppresses parasitic side reactions with the electrolyte. As a result, PVDFA-N5 enables the formation of a thin, uniform, and stable CEI layer while maintaining a microcrack-free particle morphology. This study highlights the power of rational binder engineering in simultaneously addressing mechanical degradation and interfacial instability in high-nickel cathodes.

3. Conclusion

In this study, a tough, adhesive, and protective binder system, PVDFA-N#, is developed to address the mechanical and interfacial challenges of high-nickel layered oxide cathodes. By systematically tuning the cross-linking density of the PVDFA-N system, the mechanical properties of the binder are optimized, achieving high toughness and strong adhesion. The optimized PVDFA-N5 binder enables the formation of a uniform, crack-free cathode structure and maintains strong interfacial contact with NCM particles, even under high mass loading (≈28 mg cm^{-2}) and lean binder conditions (2 wt.%). Importantly, this work demonstrates a new perspective on binder functionality, showing that the binder not only provides mechanical adhesion but also actively serves as a protective shield at the electrode-electrolyte interface. Post-mortem analyses after cycling reveal that the PVDFA-N5 binder forms a conformal interfacial layer that effectively suppresses structural degradation, transition metal ion dissolution, and inhomogeneous CEI formation. DFT calculations further confirm that the synergistic coordination by carboxyl and amine groups enhances metal ion chelation, contributing to improved interfacial stability. As a result, the PVDFA-N5 cathode achieves excellent long-term cycling performance, retaining ≈80% of its initial capacity after 300 cycles and maintaining stable operation beyond 600 cycles. This study highlights the critical importance of rational binder design, moving beyond conventional adhesion strategies toward multifunctional protective shields. Such an approach opens a new avenue for engineering durable, high-energy lithium-ion batteries through molecular-level interfacial stabilization of high-Ni cathodes, enabled by advanced binder architectures.

4. Experimental Section

Materials: Branched polyethyleneimine (PEI, average $M_w \approx 25{,}000$ g mol^{-1} and $M_n \approx 10{,}000$ g mol^{-1}), polyvinylidene fluoride (PVDF, average $M_w \approx 534{,}000$ g mol^{-1}), and 1,1,4,7,10,10-hexamethyltriethylenetetramine (HMTETA) were purchased from Aldrich. 1-Methyl-2-pyrrolidone (NMP), *tert*-butyl acrylate (tBA), copper(I) chloride (CuCl), hydrochloric acid (HCl), and 1,4-dioxane were purchased from TCI. 1.2 м Lithium hexafluorophosphate ($LiPF_6$) in a mixture of ethylene carbonate (EC) and ethyl methyl carbonate (EMC) (3:7 vol%) with 2 wt.% of vinylene carbonate (VC) and 10 wt.% of fluoroethylene carbonate (FEC) was purchased from Welcos Co., Ltd (Korea). Li metal chip (thickness: 250 μm, diameter: 16 mm) and coin cell components were purchased from MTI Korea. Trilayer polypropylene/polyethylene/polypropylene (PP/PE/PP, Celgard2320, thickness: 20 µm) was used as a separator for electrochemical analyses. All other chemicals and solvents were purchased from reliable commercial sources and used as received.

Synthesis of PAA-Grafted PVDF (PVDF-g-PAA) (PVDFA): PVDFA was synthesized by atom transfer radical polymerization (ATRP). PVDF (1.00 g, 15.6 mmol of VDF group) was dissolved in NMP to prepare a 10 wt.% solution, and the solution was mixed with CuCl (0.010 g, 0.100 mmol), and HMTETA (0.047 g, 0.21 mmol) were dissolved in 22.9 mL of tBA and added to a one-neck flask equipped with a magnetic stirring bar. The flask was purged with argon gas for 15 min before being immersed in an oil bath thermostated at 100 °C, and polymerization was conducted for 17 h. The reaction was quenched by liquid nitrogen, followed by precipitation in methanol two times. After being dried under a dynamic vacuum at 30 °C overnight, a slightly brownish powder was obtained. The obtained polymer (1.00 g, 13.1 mmol of VDFA) and HCl (0.360 g, 9.90 mmol) were dissolved in 19.4 mL of 1,4-dioxane and added to a one-neck flask equipped with a magnetic stirring bar. The reaction was conducted at 60 °C for 20 h, and the crude product was precipitated in distilled water two times. After being dried under a dynamic vacuum overnight, PVDFA was obtained with a yield of 80%.

Preparation of Pre-Binder Solution: A series of pre-binder solutions before curing was prepared by dissolving PVDFA and PEI in NMP. Note that the resulting pre-binder is designated as PVDFA-N#, where the number # indicates the mol% of amine groups in PEI along the VDF repeating units of PVDFA. The following representative procedure was for preparing PVDFA-N5. PVDFA (0.200 g, 3.16 mmol of VDF group) and PEI (7.00 mg, 0.158 mmol of amine group) were dissolved in 3.97 mL of NMP and magnetically stirred at 40 °C for 18 h until a homogeneous solution was obtained.

Preparation of NCM811 Cathodes: $LiNi_{0.8}Co_{0.1}Mn_{0.1}O_2$ (NCM811) (80 wt.%) was used as a cathode active material and dispersed in NMP with Super P (10 wt.%) and pre-binder (PVDFA-N#) solution (10 wt.%) using a Thinky mixer. The resultant slurry was uniformly cast onto an aluminum (Al) current collector using a doctor blade, followed by drying under a dynamic vacuum condition at 120 °C overnight. The dried electrode was roll-pressed at room temperature, resulting in a thickness reduction of 30% (70% of its original thickness). The mass loading of the active materials in the NCM cathode was approximately in the range of 10–11 mg cm^{-2} and 25–28 mg cm^{-2} for low and high mass loading cathodes, respectively.

Preparation of Graphite Anode: Graphite (MTI Korea) (90 wt.%) was used as an anode active material and dispersed in NMP with Super P (5 wt.%) and PVDF (5 wt.%) using a Thinky mixer. The resultant slurry was cast onto a copper current collector using a doctor blade, followed by vacuum drying at 120 °C to remove the residual NMP. The dried electrode was roll-pressed at 30 °C, resulting in a thickness reduction of 20% (80% of its original thickness).

Density Functional Theory (DFT) Calculation: All molecular structures were optimized using DFT at the B3LYP/6-311++G (d,p) level of theory with Grimme's DFT-D3 dispersion correction (zero damping), as implemented in Gaussian 16. Single-point energy calculations were subsequently performed using the B3LYP functional and the def2-TZVP basis set for enhanced accuracy. The conductor-like polarized continuum model (CPCM) was employed to account for the dielectric environment, with the dielectric constant at 30.28 to reflect the EC/EMC-based electrolyte solvent composition. The binding energy (E_b) between two components was determined by:

$$E_b = E_{total} - (E_A + E_B) \tag{1}$$

where E_{total}, E_A, and E_B are the total energies of the A-B complex, A component, and B component, respectively.

Electrochemical Characterizations: Charge–discharge cycling tests of Li/Celgard 2320/NCM811 cell were conducted using a 2032 coin cell at a cut-off voltage range of 3.0–4.3 V (vs Li/Li$^+$) at 30 °C unless otherwise noted, where 1 C corresponds to a current density of 200 mA g^{-1}. Before the main cycling, all the cells were subjected to three formation cycles at 0.1 C during the charge–discharge process. Subsequent cycling was performed at 0.5 C for charging and discharging. 1.2 м $LiPF_6$ in EC:EMC (3:7 vol%) with 2 wt.% VC and 10 wt.% FEC was used as a liquid electrolyte. Electrochemical impedance spectroscopy (EIS) was performed using a ZIVE MP1 multichannel workstation (WonATech Co., Korea) in a frequency range from 0.1 to 1 MHz with 10 mV of amplitude at 30 °C. All the cell components were assembled in an argon-filled glove box (O_2 < 0.1 ppm, H_2O < 0.1 ppm). Cyclic voltammetry (CV) was performed using a ZIVE MP1 multichannel workstation (WonATech Co., Korea) in a voltage range of 2.0–4.3 V (vs Li/Li$^+$) at a scan rate ranging from 0.3 to 1.1 mV s^{-1}. Galvanostatic intermittent titration technique (GITT) was conducted by applying a constant current pulse of 0.1 C for 10 min, followed by an open-circuit relaxation period of 50 min, within a voltage range of 3.0–4.3 V during both the charge and discharge process.

Instrumentation and Characterization Techniques: ^{1}H nuclear magnetic resonance (NMR) spectra were recorded on an AvanceIII HD spectrometer (300 MHz) installed at the National Center for Inter-university Research Facilities (NCIRF) at Seoul National University, using acetone-d_6 and DMSO-d_6 (Cambridge Isotope Laboratories) as the solvents at room temperature, with tetramethylsilane (TMS) as a reference. The Fourier-transform infrared (FT-IR) spectra were recorded in the absorption mode on a Nicolet 6700 FT-IR spectrometer with a resolution of 4 cm^{-1} in the vibrational frequency range from 400 to 4000 cm^{-1}. X-ray diffraction (XRD) measurements were conducted at the X-ray powder diffractometer (Rigaku SmartLab Corp, Japan) in the range from 10° to 90° with Cu Kα radiation at 3 kW. The tensile tests were conducted using the Lloyd-LS1+ universal tensile machine (Lloyd, UK) with a cross-head speed of 10 mm min^{-1}. The polymer films were cut into dog-bone-shaped specimens using the ASTM standard D638-M (type V specimens), and at least five measurements were performed for each sample to determine the reliable average values. The 180° adhesion tests were carried out using a Lloyd-LS1+ with a cross-head speed of 30 mm min^{-1}. The 3 м double-sided tape was attached to the electrode samples with a dimension of 1.2 × 2.0 cm^2 using a rubber roller (diameter: 95 mm, width: 45 mm, weight: 2.0 kg) to ensure consistent pressure throughout the experiments. The adhesion strength was recorded upon peeling at a 180° angle. The peeling force of the cathode at 10 µm depth was determined by surface and interfacial cutting analysis system (SAICAS) installed at the National Center for Inter-university Research Facilities (NCIRF) at Seoul National University using the SAICAS EN-EX (Daipla Wintes Co., Ltd., Japan). A blade (width: 1 mm) fixed with a shear angle of 45°, rake angle of 20°, and clearance angle of 10° moved with a horizontal velocity of 5 μm s^{-1} for 200 s. The peeling force was determined by the following equation:

$$P\left(\mathrm{kN\ m^{-1}}\right) = F_{\mathrm{h,avg}}\ (\mathrm{N})\ /w\ (\mathrm{mm}) \tag{2}$$

where P is the peeling force, $F_{\mathrm{h,avg}}$ is the average value of horizontal force after peeling, and w is the width of the blade. X-ray photoelectron spectroscopy (XPS) was performed using an ESCA II Axis Supra (Kratos, U.K.) with a monochromatized Al Kα as a radiation source (15 keV, 20 mA). A survey spectrum was collected over a range of 0–1400 eV, followed by high-resolution narrow scans of C1s, F1s, and Ni2p regions. Depth profiles were collected using an Ar$^+$ sputter source with a sputter rate of 0.2 nm min^{-1}. Field-emission scanning electron microscopy (FE-SEM) was performed on a GeminiSEM 560 (Zeiss company, Germany) installed at the National Center for Inter-university Research Facilities (NCIRF) at Seoul National University, at an accelerating voltage of 2 kV. The SEM specimens were prepared by washing with dimethyl carbonate (DMC), followed by vacuum drying at room temperature in an argon-filled glove box. A focused ion beam (FIB, Helios NanoLab650, FEI, US) was used to prepare scanning transmission electron microscopy (STEM) samples. The Cs corrected STEM (Probe Corrector) was performed on JEM-ARM200F (JEOL company, Japan) installed at the National Center for Inter-university Research Facilities (NCIRF) at Seoul National University. FE-TEM characterization of materials was carried out with a JEOL/JEM-F200 (TFEG) electron microscope operating at 200 kV. Samples for the TEM analyses were prepared by dispersing the powdered samples in ethanol (1 mg mL^{-1}) and adding a few drops of the resulting suspension to a carbon-coated Cu TEM grid. Time-of-flight secondary ion mass spectrometry (TOF-SIMS) was performed using a TOF.SIMS 5 (ION-TOF, Germany) with a raster size of 100 × 100 μm^2. A Bi$^+$ beam (30 keV, 1 pA) was used to analyze the depth profile, and a Cs$^+$ beam (2 keV, 120 nA) was used to sputter the electrodes with a sputtering rate of 0.2 nm s^{-1}. Cycled Li metal anodes were immersed in fresh DMC for 24 h in an argon-filled glove box before inductively coupled plasma mass spectrometry (ICP-MS, NexION 350D, Perkin-Elmer SCIEX) measurement. After removing DMC by vacuum, the amount of dissolved transition metal ions was determined by ICP-MS.

Supporting Information

Supporting Information is available from the Wiley Online Library or from the author.

Acknowledgements

This work was supported by the National Research Foundation of Korea (NRF) grant funded by the Korea government (MSIT) (No. RS-2023-00209631). This research was also supported by the “Science Education in Infosphere (SEI)” funded by the four-stage BK21.

Conflict of Interest

The authors declare no conflict of interest.

Data Availability Statement

The data that support the findings of this study are available on request from the corresponding author upon reasonable request.

Keywords

adhesion, high-nickel cathodes, interfacial stability, polymer binders, protective shield

Received: May 20, 2025
Revised: July 14, 2025
Published online:

---

[1] J.-H. Kim, N.-Y. Kim, Z. Ju, Y.-K. Hong, K.-D. Kang, J.-H. Pang, S.-J. Lee, S.-S. Chae, M.-S. Park, J.-Y. Kim, G. Yu, S.-Y. Lee, *Nat. Energy* **2025**, *10*, 295.
[2] C. Wang, C. Yang, Z. Zheng, *Adv. Sci.* **2022**, *9*, 2105213.
[3] J. Xu, X. Cai, S. Cai, Y. Shao, C. Hu, S. Lu, S. Ding, *Energy Environ. Mater.* **2023**, *6*, 12450.
[4] W. Li, E. M. Erickson, A. Manthiram, *Nat. Energy* **2020**, *5*, 26.
[5] A. Manthiram, J. C. Knight, S.-T. Myung, S.-M. Oh, Y.-K. Sun, *Adv. Energy Mater.* **2016**, *6*, 1501010.
[6] P. Hou, J. Yin, M. Ding, J. Huang, X. Xu, *Small* **2017**, *13*, 1701802.
[7] M. Jiang, D. L. Danilov, R.-A. Eichel, P. H. L. Notten, *Adv. Energy Mater.* **2021**, *11*, 2103005.
[8] T. Xu, J. Wu, J. Ding, Y. Huang, Y. Huang, W. Zhao, *ChemElectroChem* **2024**, *11*, 202300802.
[9] S. Sharifi-Asl, J. Lu, K. Amine, R. Shahbazian-Yassar, *Adv. Energy Mater.* **2019**, *9*, 1900551.
[10] J. U. Choi, N. Voronina, Y.-K. Sun, S.-T. Myung, *Adv. Energy Mater.* **2020**, *10*, 2002027.
[11] J. Xiao, N. Adelstein, Y. Bi, W. Bian, J. Cabana, C. L. Cobb, Y. Cui, S. J. Dillon, M. M. Doeff, S. M. Islam, K. Leung, M. Li, F. Lin, J. Liu, H. Luo, A. C. Marschilok, Y. S. Meng, Y. Qi, R. Sahore, K. G. Sprenger, R. C. Tenent, M. F. Toney, W. Tong, L. F. Wan, C. Wang, S. E. Weitzner, B. Wu, Y. Xu, *Nat. Energy* **2024**, *9*, 1463.
[12] J. Xu, *Nano Micro Lett.* **2022**, *14*, 166.
[13] Y.-K. Sun, S.-T. Myung, B.-C. Park, J. Prakash, I. Belharouak, K. Amine, *Nat. Mater.* **2009**, *8*, 320.
[14] X. Xu, L. Xiang, L. Wang, J. Jian, C. Du, X. He, H. Huo, X. Cheng, G. Yin, *J. Mater. Chem. A* **2019**, *7*, 7728.
[15] H. Yang, H.-H. Wu, M. Ge, L. Li, Y. Yuan, Q. Yao, J. Chen, L. Xia, J. Zheng, Z. Chen, J. Duan, K. Kisslinger, X. C. Zeng, W.-K. Lee, Q. Zhang, J. Lu, *Adv. Funct. Mater.* **2019**, *29*, 1808825.
[16] W. Cho, Y. J. Lim, S.-M. Lee, J. H. Kim, J.-H. Song, J.-S. Yu, Y.-J. Kim, M.-S. Park, *ACS Appl. Mater. Interfaces* **2018**, *10*, 38915.
[17] F. Xin, H. Zhou, X. Chen, M. Zuba, N. Chernova, G. Zhou, M. S. Whittingham, *ACS Appl. Mater. Interfaces* **2019**, *11*, 34889.
[18] G. Hu, Y. Tao, Y. Lu, J. Fan, L. Li, J. Xia, Y. Huang, Z. Zhang, H. Su, Y. Cao, *ChemElectroChem* **2019**, *6*, 4773.
[19] M. Du, Z.-L. Hao, Y. Liu, M.-Y. Ma, J.-L. Yang, Z.-X. Huang, Z.-Y. Gu, K.-Y. Zhang, J.-Z. Guo, X.-L. Wu, *ACS Appl. Mater. Interfaces* **2025**, *17*, 19230.
[20] A. M. Boyce, D. J. Cumming, C. Huang, S. P. Zankowski, P. S. Grant, D. J. L. Brett, P. R. Shearing, *ACS Nano* **2021**, *15*, 18624.
[21] T. Qin, H. Yang, Q. Li, X. Yu, H. Li, *Ind. Chem. Mater.* **2024**, *2*, 191.
[22] D. Jeong, D.-S. Kwon, H. J. Kim, J. Shim, *Adv. Energy Mater.* **2023**, *13*, 2302845.
[23] N. Park, M. Lee, H. Jung, J. Nam, *J. Power Sources* **2024**, *608*, 234607.
[24] A. Kraytsberg, Y. Ein-Eli, *Adv. Energy Mater.* **2016**, *6*, 1600655.
[25] R. Li, W. Li, A. Singh, D. Ren, Z. Hou, M. Ouyang, *Energy Storage Mater.* **2022**, *52*, 395.
[26] R. Elango, A. Demortière, V. De Andrade, M. Morcrette, V. Seznec, *Adv. Energy Mater.* **2018**, *8*, 1703031.
[27] Q. He, J. Ning, H. Chen, Z. Jiang, J. Wang, D. Chen, C. Zhao, Z. Liu, I. F. Perepichka, H. Meng, W. Huang, *Chem. Soc. Rev.* **2024**, *53*, 7091.
[28] F. Zou, A. Manthiram, *Adv. Energy Mater.* **2020**, *10*, 2002508.
[29] S.-L. Chou, Y. Pan, J.-Z. Wang, H.-K. Liu, S.-X. Dou, *Phys. Chem. Chem. Phys.* **2014**, *16*, 20347.
[30] Z. Liu, T. Dong, P. Mu, H. Zhang, W. Liu, G. Cui, *Chem. Eng. J.* **2022**, *446*, 136798.

[31] X. Liang, Q. Dong, S. Guo, C. Zeng, Z. Chen, B. Zhang, C. Zhou, J. Zhang, Z. Xing, X. Tian, X. Shi, *Adv. Energy Mater.* **2025**, *15*, 2500673.
[32] B. Jin, Z. Cui, A. Manthiram, *Angew. Chem., Int. Ed.* **2023**, *62*, 202301241.
[33] Y. Zhang, Y. Song, J. Liu, *Small* **2024**, *20*, 2307227.
[34] L. Gao, B.-L. Hu, L. Wang, J. Cao, R. He, F. Zhang, Z. Wang, W. Xue, H. Yang, R.-W. Li, *Science* **2023**, *381*, 540.
[35] Y. J. Shin, S. J. Kang, H. J. Jung, Y. J. Park, I. Bae, D. H. Choi, C. Park, *ACS Appl. Mater. Interfaces* **2011**, *3*, 582.
[36] X. Yao, X. Song, F. Zhang, J. Ma, H. Jiang, L. Wang, Y. Liu, E. H. Ang, H. Xiang, *ChemElectroChem* **2022**, *9*, 202200390.
[37] N. An, X. Wang, Y. Li, L. Zhang, Z. Lu, J. Sun, *Adv. Mater.* **2019**, *31*, 1904882.
[38] D. Jeong, J. Yook, D.-S. Kwon, J. Shim, J.-C. Lee, *Adv. Sci.* **2023**, *10*, 2302027.
[39] Z. Gong, G. Zhang, X. Zeng, J. Li, G. Li, W. Huang, R. Sun, C. Wong, *ACS Appl. Mater. Interfaces* **2016**, *8*, 24030.
[40] J. P. Gong, *Soft Matter* **2010**, *6*, 2583.
[41] B. Koo, H. Kim, Y. Cho, K. T. Lee, N.-S. Choi, J. Cho, *Angew. Chem., Int. Ed.* **2012**, *51*, 8762.
[42] L. Zhang, L. Zhang, L. Chai, P. Xue, W. Hao, H. Zheng, *J. Mater. Chem. A.* **2014**, *2*, 19036.
[43] C. Sun, H. Zhang, P. Mu, G. Wang, C. Luo, X. Zhang, C. Gao, X. Zhou, G. Cui, *ACS Nano* **2024**, *18*, 2475.
[44] J.-H. Lee, U. Paik, V. A. Hackley, Y.-M. Choi, *J. Power Sources* **2006**, *161*, 612.
[45] D. W. Aubrey, S. Ginosatis, *J. Adhes.* **1981**, *12*, 189.
[46] L. Zhong, Y. Sun, K. Shen, F. Li, H. Liu, L. Sun, D. Xie, *Small* **2024**, *20*, 2407297.
[47] K. Kim, S. Byun, J. Choi, S. Hong, M.-H. Ryou, Y. M. Lee, *ChemPhysChem* **2018**, *19*, 1627.
[48] B. Jin, A. Dolocan, C. Liu, Z. Cui, A. Manthiram, *Angew. Chem., Int. Ed.* **2024**, *63*, 202408021.
[49] R. Zhang, C. Wang, M. Ge, H. L. Xin, *Nano Lett.* **2022**, *22*, 3818.
[50] J. Jang, J. Ahn, J. Ahn, U. Jeong, J. Yoon, J. K. Park, W. Shin, M. J. Kang, M.-k. Cho, D. J. Kang, J. Kim, J.-K. Yoo, H.-G. Im, *Adv. Funct. Mater.* **2024**, *34*, 2410866.
[51] T. Liu, R. Parekh, P. Mocny, B. P. Bloom, Y. Zhao, S. Y. An, B. Pan, R. Yin, D. H. Waldeck, J. F. Whitacre, K. Matyjaszewski, *ACS Mater. Lett.* **2023**, *5*, 2594.
[52] E. Trevisanello, R. Ruess, G. Conforto, F. H. Richter, J. Janek, *Adv. Energy Mater.* **2021**, *11*, 2003400.
[53] N.-Y. Kim, J. Moon, M.-H. Ryou, S.-H. Kim, J.-H. Kim, J.-M. Kim, J. Bang, S.-Y. Lee, *Adv. Energy Mater.* **2022**, *12*, 2102109.
[54] C. Zou, Y. Huang, L. Zhao, W. Ren, Z. Zhao, J. Liu, X. Li, M. Wang, B. Guo, Y. Lin, *ACS Appl. Mater. Interfaces* **2022**, *14*, 14226.
[55] X.-F. Yang, H.-B. Zhu, M. Liu, *Polyhedron* **2017**, *128*, 18.
[56] L. Rulíšek, Z. Havlas, *J. Am. Chem. Soc.* **2000**, *122*, 10428.
[57] M. A. Treto-Suárez, J. Tapia, Y. Hidalgo-Rosa, D. Páez-Hernández, E. Molins, X. Zarate, E. Schott, *J. Phys. Chem. A* **2020**, *124*, 6493.
[58] S. Kim, S. O. Park, M.-Y. Lee, J.-A. Lee, I. Kristanto, T. K. Lee, D. Hwang, J. Kim, T.-U. Wi, H.-W. Lee, S. K. Kwak, N.-S. Choi, *Energy Storage Mater.* **2022**, *45*, 1.
[59] W. Zhao, J. Zheng, L. Zou, H. Jia, B. Liu, H. Wang, M. H. Engelhard, C. Wang, W. Xu, Y. Yang, J.-G. Zhang, *Adv. Energy Mater.* **2018**, *8*, 1800297.
[60] X. Xiong, D. Ding, Y. Bu, Z. Wang, B. Huang, H. Guo, X. Li, *J. Mater. Chem. A* **2014**, *2*, 11691.
[61] W. Li, A. Dolocan, P. Oh, H. Celio, S. Park, J. Cho, A. Manthiram, *Nat. Commun.* **2017**, *8*, 14589.
[62] H. H. Sun, A. Dolocan, J. A. Weeks, A. Heller, C. B. Mullins, *ACS Nano* **2020**, *14*, 17142.